Contents lists available at ScienceDirect

Solid State Nuclear Magnetic Resonance

Combining heteronuclear correlation NMR with spin-diffusion to detect relayed Cl–H–H and N–H–H proximities in molecular solids

Parth Raval [a], Julien Trébosc [b], Tomasz Pawlak [c], Yusuke Nishiyama [d,e], Steven P. Brown [f,**], G.N. Manjunatha Reddy [a,*]

[a] *University of Lille, CNRS, Centrale Lille Institut, Univ. Artois, UMR 8181−UCCS− Unité de Catalyse et Chimie du Solide, F, 59000, Lille, France*
[b] *Univ. Lille, CNRS, INRAE, Centrale Lille, Univ. Artois, FR 2638 - IMEC – Institut Michel-Eugène Chevreul, F, 59000, Lille, France*
[c] *Centre of Molecular and Macromolecular Studies, Polish Academy of Sciences, Sienkiewicza 112, 90-363, Lodz, Poland*
[d] *RIKEN-JEOL Collaboration Centre, RIKEN, Yokohama Campus, Yokohama, Kanagawa, 230-0045, Japan*
[e] *JEOL RESONANCE Inc., Akishima, Tokyo, 196-8558, Japan*
[f] *Department of Physics, University of Warwick, Coventry, CV4 7AL, UK*

ARTICLE INFO

ABSTRACT

Analysis of short-to-intermediate range intermolecular interactions offers a great way of characterizing the solid-state organization of small molecules and materials. This can be achieved by two-dimensional (2D) homo- and heteronuclear correlation NMR spectroscopy, for example, by carrying out experiments at high magnetic fields in conjunction with fast magic-angle spinning (MAS) techniques. But, detecting 2D peaks for heteronuclear dipolar coupled spin pairs separated by greater than 3 Å is not always straightforward, particularly when low-gamma quadrupolar nuclei are involved. Here, we present a 2D correlation NMR experiment that combines the advantages of heteronuclear-multiple quantum coherence (HMQC) and proton-based spin-diffusion (SD) pulse sequences using radio-frequency-driven-recoupling (RFDR) to probe inter and intramolecular ^{1}H-X (X = ^{14}N, ^{35}Cl) interactions. This experiment can be used to acquire 2D ^{1}H{X}-HMQC filtered ^{1}H–^{1}H correlation as well as 2D ^{1}H-X HMQC spectra. Powder forms of dopamine·HCl and L-histidine·HCl·H$_2$O are characterized at high fields (21.1 T and 18.8 T) with fast MAS (60 kHz) using the 2D HMQC-SD-RFDR approach. Solid-state NMR results are complemented with NMR crystallography analyses using the gauge-including projector augmented wave (GIPAW) approach. For histidine·HCl·H$_2$O, 2D peaks associated with ^{14}N–^{1}H–^{1}H and ^{35}Cl–^{1}H–^{1}H distances of up to 4.4 and 3.9 Å have been detected. This is further corroborated by the observation of 2D peaks corresponding to ^{14}N–^{1}H–^{1}H and ^{35}Cl–^{1}H–^{1}H distances of up to 4.2 and 3.7 Å in dopamine·HCl, indicating the suitability of the HMQC-SD-RFDR experiments for detecting medium-range proximities in molecular solids.

1. Introduction

Solid-state (ss)NMR spectroscopy is widely used to characterize the local structures and dynamics of molecular solids today. Site selectivity, natural isotopic abundance of several NMR active nuclei, and availability of a large pool of one- (1D) and two-dimensional (2D) pulse sequences to carry out homo and heteronuclear correlation experiments are among the unique capabilities of ssNMR spectroscopy for characterizing the solid form. Applications have been presented in the areas of optoelectronics, catalysis, biomacromolecules, pharmaceutical formulations, energy harvesting and storage materials [1–7]. In addition,

ssNMR, in conjunction with diffraction-based techniques and modelling approaches (also referred to as NMR crystallography), is increasingly applied to characterize the intermolecular interactions and to determine the three-dimensional structures of (semi)crystalline and amorphous solids [8–18].

The vast majority of ssNMR-based structure elucidation studies involve the analysis of chemical shifts and dipolar couplings and often quadrupolar interactions [3]. The chemical shifts are sensitive to local bonding environments, and the dipolar couplings are sensitive to interatomic distances and site-specific dynamics. Information on the isotropic chemical shifts of spin-half nuclei such as ^{1}H, ^{19}F, ^{13}C, and ^{15}N

---

can be obtained by acquiring and analyzing 1D magic-angle spinning (MAS) spectra. In addition, 2D homo- and hetero-nuclear correlation (HETCOR) experiments provide information on through-space proximities and dipolar interactions that can be used to estimate interatomic distances and molecular conformations, which help to determine the 3D structures of molecular solids. For example, double-quantum (DQ) peaks can be excited and detected for ^{1}H–^{1}H spin pairs at sub-nanometer (within 5 Å) distances, and ^{1}H–^{1}H spin-diffusion (SD) and cross-polarization (CP)-based ^{1}H-X (e.g., X = ^{13}C, ^{15}N, ^{19}F) HETCOR experiments enable the interatomic proximities to be probed within, or even beyond a nanometer. For 2D experiments involving both spin-half and quadrupolar nuclei, heteronuclear multiple-quantum coherence (HMQC)-type or insensitive nuclei enhancement by polarization transfer (INEPT)-type experiments have been used to efficiently transfer the polarization from spin-half nuclei to quadrupolar nuclei [19–25]. For example, N–H proximities can be probed at natural abundance (^{14}N spin 1, 99.6% natural isotopic abundance) using *J*-couplings (*J*-HMQC), dipolar couplings (*D*-HMQC), and using overtone (OT) ^{14}N transitions [23,25–33]. Specifically, 2D HMQC experiments have been applied to characterize ^{14}N–^{1}H proximities [28,34–38] as well as ^{35}Cl–^{1}H proximities [38–42] in small molecules and pharmaceutical solids.

To take full advantage of NMR analysis of molecular solids, it is important to probe packing interactions in the sub-nanometer to nanometer range, or even greater than a nanometer distance. Gaining access to the intermediate-range (1–10 nm) length scale is particularly important to fill the gap between the structural analysis enabled by the short-range probes (e.g., conventional magnetic resonance spectroscopy probes local structures at sub-nanometer distances) and the long-range techniques such as X-ray scattering and electron microscopy that offer morphological and structural information at tens to hundreds of nanometers regimes. For example, it has been feasible to probe intermediate-to-long range distances via spin-diffusion experiments by making use of spin magnetization exchange between nuclei at high natural abundance such as ^{1}H and ^{19}F due to the strong dipolar interactions between them, or between isotopically enriched nuclei [43–51]. Several structural elucidation studies benefit from the analysis of such intermediate-range to long-range structures, including catalytic surfaces, reactive interfaces in stacked thin films in optoelectronic devices, bio-macromolecules, polymers, functional supramolecular assemblies, and pharmaceutical formulations [44,52–64]. Notably, analysis of spin-diffusion build-up curves in conjunction with computational modelling has been used to determine three-dimensional structures of small to moderately sized molecules [47,48,65–68]. Since these molecular systems contain both spin-half and quadrupolar nuclei, detecting 2D NMR peaks for heteronuclear ^{1}H-X spin-pairs involving low-gamma quadrupolar nuclei (X = ^{14}N, ^{35}Cl), probing long-range proximities of up to 5 Å or beyond is difficult due to the weak heteronuclear dipolar interactions. Thus, a combination of features involving a 2D HMQC-type experiment and ^{1}H–^{1}H spin diffusion to probe the short-to-medium range interactions is expected to facilitate structure elucidation in organic solids and materials.

Here we combine HMQC and SD using RFDR pulse sequence elements so as to probe ^{35}Cl–^{1}H–^{1}H and ^{14}N–^{1}H–^{1}H interatomic proximities in small organic molecules. Results are demonstrated for powdered compositions of L-histidine·HCl·H$_2$O and dopamine·HCl (Fig. 1). Pulse sequences used to acquire the conventional 2D HMQC and 2D HMQC-SD-RFDR experiments are shown in Fig. 2. For each sample, the ^{1}H {^{14}N} and ^{1}H{^{35}Cl}-HMQC filtering efficiency is demonstrated on 1D versions of the HMQC and HMQC-RFDR pulse sequences. Then, the ability of a ^{1}H{^{14}N/^{35}Cl}-HMQC filtered 2D ^{1}H–^{1}H spin-diffusion experiment to detect the peaks corresponding to proton pairs that are in close proximities to ^{14}N sites is illustrated. Next, proton-detected 2D ^{1}H–^{14}N and ^{1}H–^{35}Cl HMQC spectra were acquired and analyzed to demonstrate how medium-range N–H–H and Cl–H–H correlations are observed for the interatomic N–H and Cl–H distances reaching and exceeding 4 Å. The solid-state NMR results are correlated and
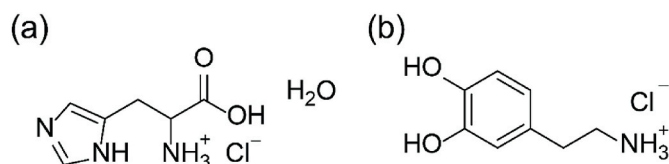

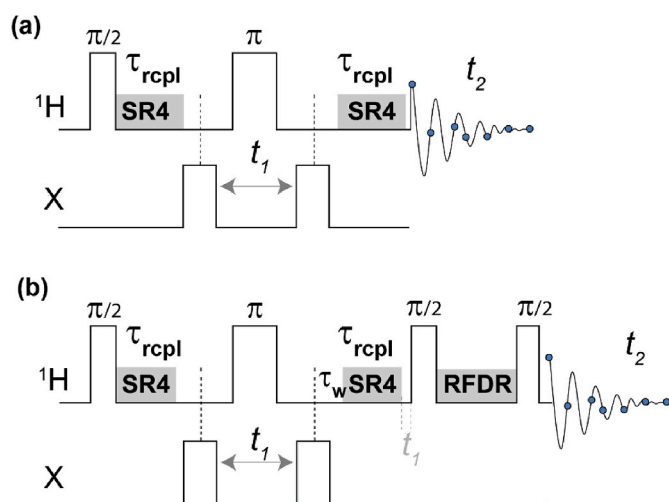**Fig. 1.** Chemical structures of L-histidine·HCl·H$_2$O and dopamine·HCl.

Fig. 2. Pulse sequences used to acquire two-dimensional (a) HMQC and (b) HMQC-SD-RFDR spectra. The sequence shown in (b) can be used to acquire ^{1}H {X}-filtered ^{1}H–^{1}H SD correlations spectra as well as ^{1}H-X HMQC-SD-RFDR correlation spectra, depending on the placing of the t_1 evolution period. In both cases, SR4$_1^2$ pulses are applied for the recoupling of ^{1}H-X (X = ^{35}Cl, ^{14}N) dipolar interactions, and in (b), an RFDR block is added to enhance the spin diffusion process leading to a ^{1}H-detected 2D experiment. The evolution during t_1 and the ^{1}H RFDR pulses during spin diffusion are rotor-synchronized with respect to the sample spinning.

complemented by periodic density functional theory calculations using the gauge-including projector augmented wave (GIPAW-DFT) approach. These results suggest that the proposed method has wider relevance in investigating the medium-range interatomic proximities between spin-half and low-gamma quadrupolar nuclei in molecular solids.

2. Experimental details

Solid-state NMR spectroscopy Powders of L-histidine·HCl·H$_2$O [C$_6$H$_9$N$_3$O$_2$·HCl·H$_2$O] and dopamine·HCl [(HO)$_2$C$_6$H$_3$(CH$_2$)$_2$NH$_2$·HCl]) were purchased from Sigma Aldrich and used as received. Approximately 2.3 mg of L-histidine·HCl·H$_2$O and dopamine·HCl were separately packed into 1.3 mm (outer diameter) rotors. All 1D ^{1}H MAS and 2D ^{1}H–^{1}H correlation experiments were performed on a Bruker Avance Neo solid-state NMR spectrometer operating at a ^{1}H Larmor frequency of 900 MHz, equipped with a 1.3 mm double-resonance MAS probe head. The ^{1}H and ^{14}N pulse lengths, dipolar recoupling periods (τ_{rcpl}), and spin diffusion times using RFDR (τ_{RFDR}) were empirically optimized using 1D versions of the HMQC and HMQC-SD-RFDR pulse sequence shown in Fig. 2. 1D ^{1}H MAS NMR spectra of L-histidine·HCl·H$_2$O and dopamine·HCl were acquired with 128 co-added transients. 1D ^{35}Cl spectra of L-histidine·HCl·H$_2$O and dopamine·HCl·H$_2$O were acquired with 512 and 4096 co-added transients using a Quadrupolar Carr-Purcell-Meiboom-Gill (QCPMG) sequence [69]. All ^{1}H chemical shifts are calibrated with respect to neat TMS using adamantane as an external reference (^{1}H resonance, 1.85 ppm) [70]. ^{14}N shifts were referenced to a saturated NH$_4$Cl aqueous solution at −352.9 ppm, corresponding to the primary reference, liquid CH$_3$NO$_2$ (0 ppm) [71]. To compare with the

alternative IUPAC reference of liquid NH_3 at -50 °C as used in protein NMR, it is necessary to add 379.5 ppm [71]. ^{35}Cl experimental shifts are referenced to 0.1 M NaCl solution in D_2O based on the IUPAC recommendation (see Table A1 in Ref. [72]).

HMQC. All 2D HMQC NMR experiments were performed on a Bruker Avance Neo (21.1 T Larmor frequency of ^{1}H = 900.2 MHz, ^{14}N = 65.0 MHz or 18.8 T Larmor frequency of ^{1}H = 800.1 MHz, ^{14}N = 57.8 MHz, and ^{35}Cl = 78.4 MHz) spectrometer, using a 1.3 mm Bruker probe operating in double-resonance mode at a 60.241 kHz MAS frequency. The pulse sequence used to acquire the ^{14}N–^{1}H HMQC spectra is reported in Fig. 2a. $SR4_1^2$ recoupling elements were used to reintroduce the heteronuclear ^{14}N–^{1}H dipolar couplings, using a duration $\tau_{rcpl} = 166$ μs. [73]. The ^{1}H π/2 pulse duration and the ^{14}N pulse durations were 2.2 μs and 16.6 μs, respectively. For each of 80 t_1 FIDs acquired using the States method to achieve sign discrimination in the indirect F_1 dimension with a rotor synchronized increment of 16.6 μs, 32 transients were coadded with a recycle delay of 2 s. A ^{1}H nutation frequency of 208.3 kHz was used for the 90° pulse in the single-pulse experiments. For L-histidine·HCl.H_2O, all the 2D ^{1}H–^{14}N and ^{1}H–^{35}Cl (HMQC and HMQC-SD-RFDR) spectra were acquired with 48 t_1 FIDs, each with 32 and 128 co-added transients, respectively. For 2D ^{1}H–^{14}N and ^{1}H–^{35}Cl correlation experiments, the total experimental times were respectively ~1 h and ~3.5 h each. For both HMQC and HMQC-RFDR sequences, a ^{1}H nutation frequency of 113.6 kHz was applied for the 90° pulse (2.2 μs) and 180° pulse (4.4 μs). A rotor-synchronized $SR4_1^2$ pulse was employed to recouple ^{1}H–^{14}N or ^{1}H–^{35}Cl dipolar interactions. For dopamine·HCl, all 1D ^{1}H MAS and ^{1}H{^{14}N} filtered 1D MAS, and 2D ^{1}H–^{14}N HMQC spectra were acquired on a Bruker Avance Neo (21.1 T, Larmor frequency of ^{1}H = 900.2 MHz, ^{14}N = 65.0 MHz) spectrometer. The ^{1}H nutation frequency was 175.4 kHz for a 90° pulse. 2D ^{1}H–^{14}N HMQC spectra were acquired with 48 t_1 FIDs, each with 32 co-added transients, corresponding to an experimental time of ~1.3 h each. 2D ^{1}H–^{35}Cl spectra were acquired with 80 t_1 FIDs, each with 128 co-added transients, corresponding to an experimental time of ~8.5 h each.

HMQC-SD-RFDR pulse sequence: To begin with, an HMQC pulse sequence (Fig. 2a) is used for the excitation and reconversion of HMQC coherences, whereby the interval between the two ^{14}N pulses are rotor synchronized with sample spinning, i.e., $t_1 = n\tau_r$, where n is an integer. During this sequence, the SR4 pulse sequence was applied during the excitation and reconversion periods to decouple the ^{1}H–^{1}H homonuclear dipolar interactions and recouple the ^{1}H–^{14}N heteronuclear dipolar interactions. To this sequence, a spin-diffusion filter is added with two 90° pulses separated by a mixing delay, also referred to as a spin diffusion delay. Since ^{1}H–^{1}H spin diffusion is suppressed when experiments are carried out at fast sample spinning (here 60 kHz MAS), radio-frequency-driven recoupling (RFDR) [74] pulses (Fig. 2b) are added within the spin diffusion filter to enhance the spin diffusion process. This leads to a ^{1}H detected 2D pulse sequence that can be applied to acquire 2D ^{1}H {^{14}N}-HMQC filtered ^{1}H–^{1}H NOESY-like spectra (by placing the t_1 evolution between the HMQC block and the spin diffusion block, as depicted in gray color) as well as 2D ^{1}H–^{14}N relay HMQC spectra. To compare the spectral filtering efficiency, spectra acquired using the 1D versions of the HMQC and HMQC-SD-RFDR experiments are compared with a single-pulse experiment in Fig. 3 and in a later section (all spectra are acquired at identical experimental conditions). The sensitivity of the conventional 1D ^{1}H{^{14}N/^{35}Cl} HMQC experiment is about 5%, and the ^{1}H{^{14}N/^{35}Cl}-HMQC-SD-RFDR experiment is about 1%, as compared to the single-pulse ^{1}H MAS experiment. Of particular note, the sensitivity of the proposed experiment depends on the relative strengths of both homo and heteronuclear dipolar couplings. For example, in both samples, the efficiency for NH_3 protons is less due to the rotational dynamics of the NH_3 group as compared to the aromatic protons. 2D HMQC-SD-RFDR experiments were acquired under identical conditions to those of conventional HMQC experiments, except the RFDR-based spin-diffusion mixing times are added as indicated in the appropriate
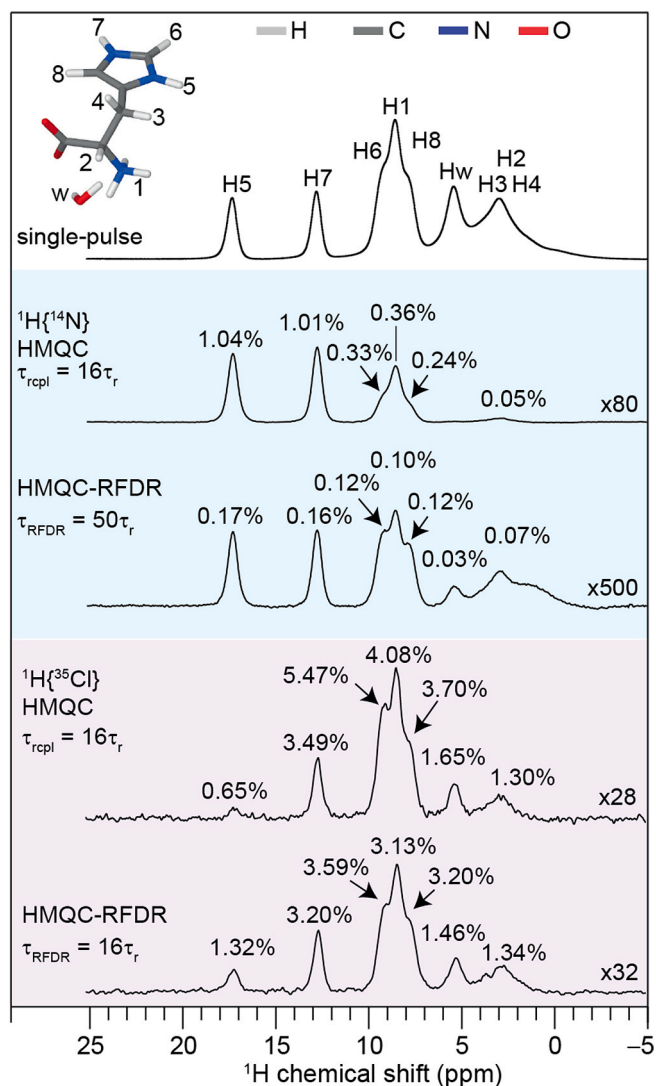
Fig. 3. Experimental ^{1}H NMR spectra are presented for L-histidine·HCl·H_2O; (top-to-bottom) a ^{1}H (800 MHz, 50 kHz MAS) single-pulse spectrum, a ^{1}H{^{14}N} HMQC-filtered ^{1}H spectrum recorded using τ_{rcpl} of 320 μs and also with τ_{RFDR} = 1000 μs, and a ^{1}H{^{35}Cl} HMQC-filtered ^{1}H spectrum (800 MHz, 60.24 kHz MAS) recorded using τ_{rcpl} = 265.6 μs and also with τ_{RFDR} = 265.6 μs.

figure captions.

Quantum mechanical calculations using a periodic-DFT approach. The molecular coordinates obtained from previously published crystal structures of L-histidine.HCl.H_2O (CCDC code: HISTCMO1) [75] and dopamine·HCl (CCDC codes for the HCl salt and zwitterionic forms are DOPAMN and TIRZAX) [76] were taken to prepare input files for the quantum mechanical calculations. The geometry optimizations of crystal structures were carried out with periodic density functional theory (DFT) calculations. For all the geometry optimized structures, the NMR chemical shifts were computed using the gauge including projected augmented wave (GIPAW) method as described by Pickard and Mauri [77,78]. All periodic DFT calculations were performed using the CASTEP 19.11 code [79]. Each self-consistent field (SCF) loop was performed until the energy was converged to within 3.67×10^{-8} Hartrees. For all calculations, the generalized density approximation DFT functional PBE with the Tkatchenko-Scheffler (TS) dispersion correction scheme (DFT-D method) was applied with ultrasoft pseudopotentials [80,81]. The maximum plane wave cut-off energy was 23.15 Hartrees. The Broyden–Fletcher–Goldfarb–Shanno (BFGS) optimization algorithm was used, and a Monkhorst−Pack grid of minimum sample spacing 0.07

× 2π Å^{-1} was applied to sample the Brillouin zone. The positions of the atoms were allowed to vary within the unit cell until the average forces, energies, and displacements remaining were below 3.6749 × 10^{-7} Hartree/Å, 0.0011025 Hartrees, and 0.001 Å, respectively. The interatomic distances for histidine.HCl.H$_2$O and dopamine·HCl molecules stated in this study correspond to the DFT optimized structures.

3. Results and discussion

L.histidine·HCl·H$_2$O: The solid-state form of L-histidine·HCl·H$_2$O, and protonated and tautomeric structures of histidine have been well characterized by ^{1}H, ^{13}C, ^{14}N/^{15}N, and ^{35}Cl MAS NMR spectroscopy in previous studies [36,38,40,82,83]. Here, we used L-histidine·HCl·H$_2$O as a control sample to test the proposed HMQC-SD-RFDR experiment. Fig. 3 compares ^{1}H MAS spectra of L-histidine·HCl·H$_2$O acquired by a single-pulse as well as 1D versions of ^{1}H{^{14}N} and ^{1}H{^{35}Cl} HMQC and HMQC-SD-RFDR pulse sequences. A single-pulse ^{1}H MAS NMR spectrum exhibits peaks at 2.8 ppm corresponding to the CH$_2$/CH sites and at 5.2 ppm originating from water molecules, and the partially resolved signals at 8.9 and 7.7 ppm are due to H6, H1, H8 sites as depicted in the schematic structure. The ^{1}H chemical shifts of hydrogen bonded protons are observed at higher frequencies (i.e., 8.4, 12.5, and 17.1 ppm): N–H (1) ⋯ O(w) hydrogen bonding interactions with oxygen atoms of water molecules, intermolecular N–H(5) ⋯ O and N–H(7) ⋯ O hydrogen-bonding interactions with the carboxylic acid groups of the neighboring histidine molecules, for which the intermolecular donor (N)-acceptor(O) distances are 2.61 and 2.78 Å, respectively. A ^{1}H–^{1}H double-quantum-single-quantum (DQ-SQ) correlation NMR spectrum together with the DQ peak assignments corresponding to ^{1}H–^{1}H distances between 3 Å and 4.5 Å is presented in Fig. S1 (Supporting Information). For the spectra acquired under identical experimental

conditions, spectral simplification and sensitivity of the ^{1}H signals achieved by ^{1}H{^{14}N} and ^{1}H{^{35}Cl} HMQC filters with respect to the single-pulse experiment are examined and compared (Fig. 3, colored shaded regions). The 1D ^{1}H{^{14}N}-HMQC filtered spectra acquired with 320 μs of SR4 recoupling time exhibited signals corresponding to the directly bonded ^{1}H–^{14}N sites, i.e., H1, H5, and H7 peaks are detected, while the signals originating from all other protons are poorly detected (or undetected). Although the addition of a spin diffusion delay leads to the exchange of magnetization from ^{1}H{^{14}N} sites to the neighboring ^{1}H sites, the proton spin-diffusion (SD) is less efficient when experiments are carried out under fast MAS [84–86]. Therefore, the RFDR pulses have been used within the spin-diffusion filter to enhance the ^{1}H–^{1}H spin-diffusion process. The addition of a SD-RFDR block (1000 μs) to the 1D HMQC experiment with the same 320 μs of SR4 recoupling time enables the weak intensity signals (H2, H3, H4, and Hw) to be detected with much higher intensities, although the intensities of H5 and H7 peaks are reduced, yielding signal uniformity like that of single-pulse experiment. A similar trend is observed for the ^{1}H{^{35}Cl} HMQC filtered spectra of L-histidine·H$_2$O·HCl, whereby the spectra acquired with 265.6 μs of SR4 recoupling time before and after the addition of RFDR (265.6 μs) showed different ^{1}H peak intensities. In the latter, the H5 and H2–H4 sites exhibited signal enhancements, as indicated in Fig. 3. A striking advantage of the SD-RFDR block is that it enables the ^{1}H signals corresponding to the dipolar coupled ^{1}H–^{1}H pairs in the vicinity of ^{14}N and ^{35}Cl sites to be detected, demonstrating the sensitivity enhancements for specific ^{14}N–^{1}H–^{1}H and ^{35}Cl–^{1}H–^{1}H sites via relay transfer.

To test the role of RFDR blocks in enhancing the ^{1}H–^{1}H spin-diffusion process to the neighboring ^{1}H sites, NOESY-like 2D ^{1}H–^{1}H NMR spectra of L-histidine·HCl·H$_2$O were acquired (21.1 T, 60 kHz MAS) with and without SD-RFDR blocks. The conventional NOESY-like 2D ^{1}H–^{1}H
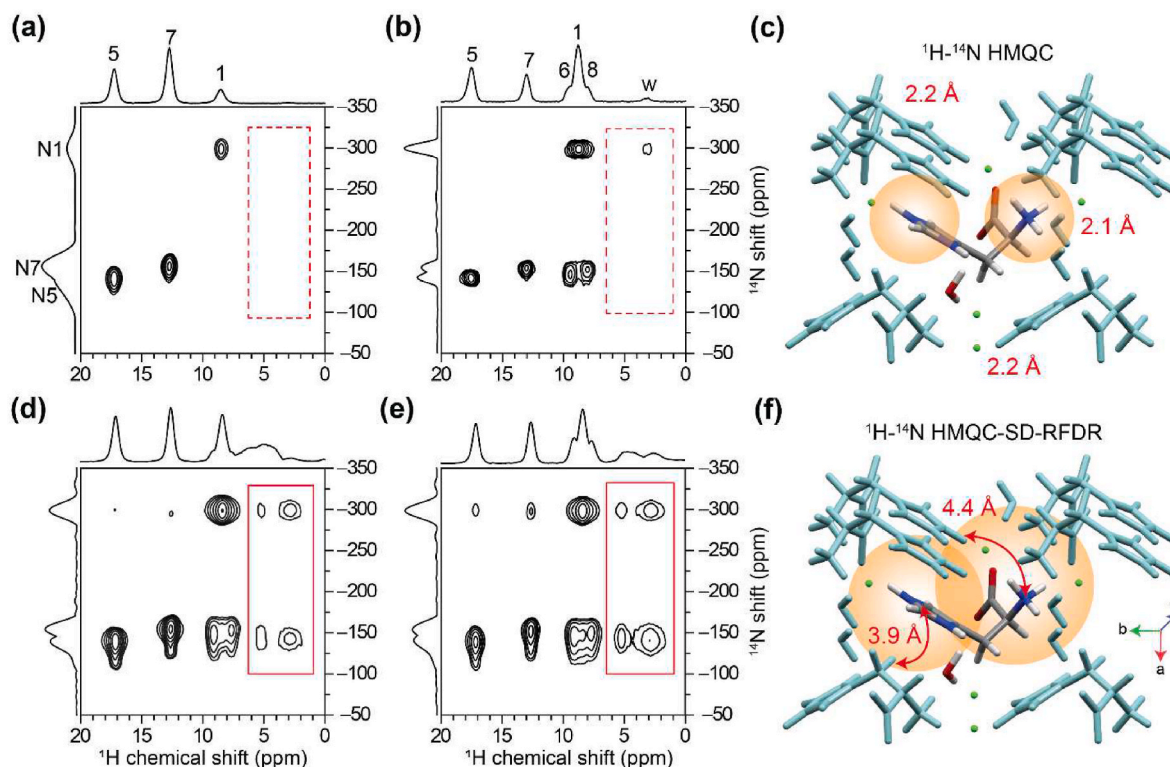
Fig. 4. Two-dimensional ^{1}H–^{14}N correlation spectra with skyline projections of L-histidine·HCl·H$_2$O acquired at 18.8 T and 60.24 kHz MAS with (a, b) conventional HMQC and (d,e) HMQC-SD-RFDR pulse sequences as shown in Fig. 2. In all cases, SR4 recoupling for a τ_{RCPL} duration of 166 μs was used except for (b) where the SR4 recoupling time was 498 μs. RFDR durations were 166 μs (d) and 498 μs (e). The base contour levels are at 6% of the maximum peak height. Representations of the periodic DFT geometry optimized structure of L-histidine·HCl·H$_2$O illustrating the short- and long-range interactions probed by the HMQC and HMQC-SD-RFDR approaches are shown in (c) and (f) with spheres representing the distances between ^{14}N and ^{1}H sites.

correlation spectra of L-histidine.HCl.H$_2$O acquired with different mixing times in the 1–100 ms range are presented in Supporting Information (Fig. S2), whereby the short mixing time of 10 ms was insufficient to exchange the magnetization between the neighboring sites, and 100 ms enabled magnetization exchange between different sites. The advantage of using RFDR blocks to enhance spin-diffusion process in 2D experiments acquired under fast MAS is demonstrated in Fig. S3. By adding an HMQC filter prior to the ^{1}H–^{1}H SD-RFDR pulse sequence, a 2D ^{1}H{^{14}N} HMQC-filtered ^{1}H–^{1}H SD spectrum can be acquired. In a HMQC-filtered 2D ^{1}H–^{1}H SD-RFDR spectrum acquired with a mixing time of 16.6 μs, i. e., one rotor period (Fig. S3c), the diagonal peaks associated with NH$_3$, H5, and H7 protons are observed. By comparison, the RFDR mixing time of 531.2 μs enabled the 2D correlation peaks between all the sites to be observed (Fig. S3d), confirming that the RFDR enhances the spin-diffusion process. It is to be noted that similar experiments can be carried out using a ^{35}Cl{^{1}H} HMQC filter to achieve spectral simplification in HCl salts of small organic molecules.

Next, 2D ^{1}H–^{14}N HMQC spectra were acquired without and with SD-RFDR pulses (Fig. 4) in order to probe N–H and N–H–H proximities. We start by analyzing the conventional 2D ^{1}H–^{14}N HMQC spectra of L-histidine.HCl.H$_2$O acquired with different ^{1}H–^{14}N recoupling times considering the molecular packing interactions in the vicinity of ^{14}N sites as obtained from the periodic DFT optimized L-histidine·HCl·H$_2$O crystal structure. In an HMQC spectrum acquired with a short recoupling time of 166 μs (Figure 4a), 2D peaks corresponding to directly bonded NH moieties are observed, including N7–H7, N5–H5 within the imidazole ring, and N1–H1 within the NH$_3^+$ group. In the 2D HMQC experiment acquired with a recoupling time of 498 μs (Fig. 4b), peaks associated with stronger (one-bond) and weaker dipolar coupled N–H sites are observed including N5–H6, N7–H6, N7–H8, and N1–H2 corresponding to the shortest N–H distances of 2.17, 2.15, 2.15 and 2.08 Å,

respectively. These distances are depicted in the periodic DFT optimized crystal structure of L-histidine·HCl·H$_2$O shown in Fig. 4c. Further increase in the recoupling time up to 800 μs (spectra not shown) yields a poor signal to noise ratio and no additional long-range N–H correlations were detected, suggesting that the conventional HMQC experiment is unable to probe through-space proximities with N–H exceeding 3 Å (dashed boxes in Fig. 4b) [87]. This is because of the dipolar-based HMQC experiment utilizing heteronuclear dipolar interactions (D_{NH}), which are an order magnitude weaker than the homonuclear proton-proton dipolar couplings (D_{HH}). For example, a through-space dipolar coupled ^{14}N–^{1}H pair separated by ~4.43 Å distance exhibits a dipolar coupling of ~100 Hz, which is too weak to produce a detectable 2D peak in the conventional HMQC spectrum. For the same ^{14}N–^{1}H heteronuclear recoupling of 166 μs, the addition of RFDR pulse of 166 μs leads to the detection of poorly dipolar coupled ^{14}N–^{1}H sites (≥3 Å): for example, 2D peaks correlating N1 and Hw, H2, H3 and H4 chemical shifts with a nearest ^{14}N to Hw distance of 3.4 Å and ^{14}N to H2, H3, H4 distances of 3.4 Å are observed. In addition, these 2D peaks are detected with much higher intensities when RFDR with a duration of 512 μs is used. This is evidenced in the HMQC-SD-RFDR spectra of L-histidine. HCl.H$_2$O (Fig. 4d and e), whereby RFDR-assisted recoupling of ^{1}H–^{1}H dipolar interactions enables medium-range ^{14}N–^{1}H–^{1}H interactions to be probed via relay transfer (solid boxes). Such relayed correlations are observed due to the magnetization transfer between strongly dipolar coupled ^{1}H–^{1}H pairs in the vicinity of ^{14}N sites and can be strengthened by utilizing the larger D_{HH} values, particularly by using ^{1}H-RFDR transfer. 2D peaks are observed for the proton pairs that are up to 4 Å away from the ^{14}N sites (Fig. 4f), suggesting that the correlations between nitrogen atoms and remote protons can be observed using this approach. It is noteworthy that 3D ^{1}H–^{1}H–^{14}N or ^{1}H–^{1}H–^{19}F correlation experiments provide identical information [36,88,89], however, the 2D
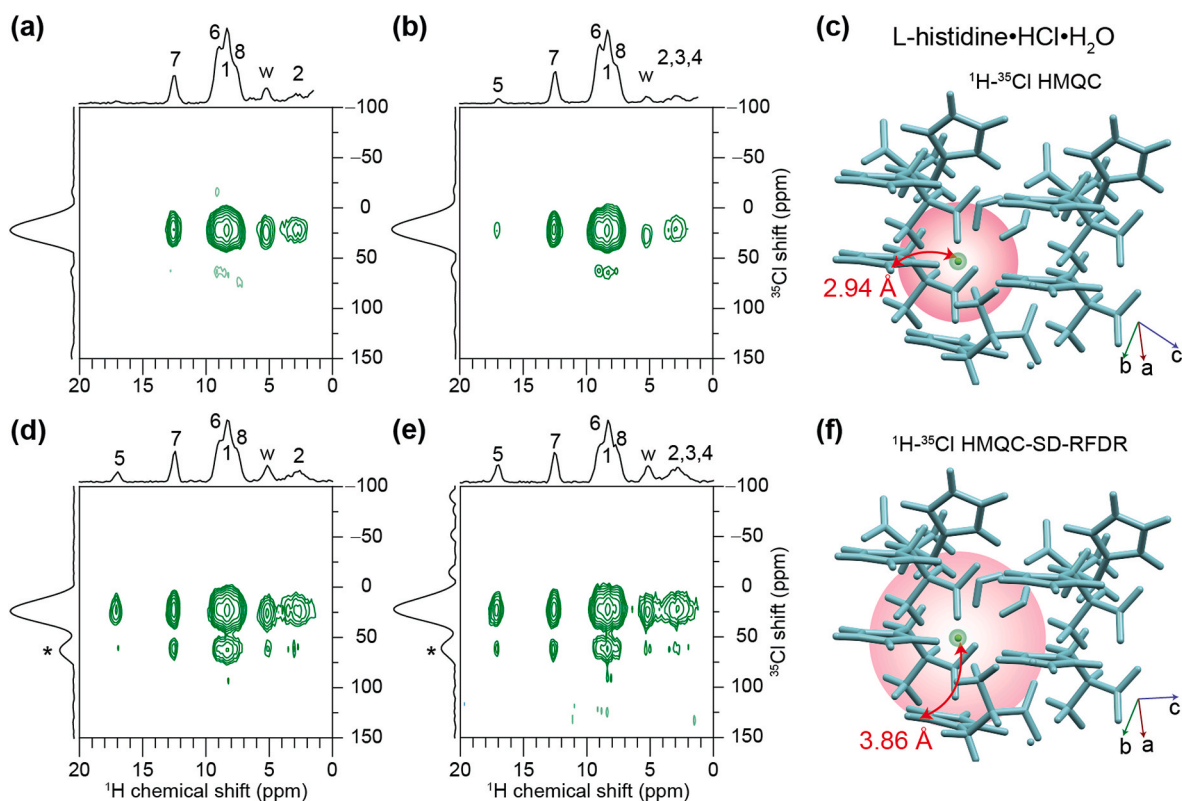

Fig. 5. Two-dimensional ^{1}H–^{35}Cl HMQC spectra with skyline projections of L-histidine·HCl·H$_2$O acquired at 18.8 T and 60.24 kHz MAS without (a, b) and with (d, e) SD-RFDR blocks. SR4 recoupling with a τ_{RCPL} duration of (a,d, and e) 265.6 μs and (b) 531.2 μs was used to reintroduce the heteronuclear ^{35}Cl–^{1}H dipolar interactions. RFDR durations were 265.6 μs (d) and 531.2 μs (e). The base contour levels are at 6% of the maximum peak height. The peak at ~59 ppm in the vertical ^{35}Cl dimension is a satellite transition. Representations of the periodic DFT geometry optimized structure of L-histidine·HCl·H$_2$O illustrating the ^{35}Cl–H and ^{35}Cl–H–H proximities probed by the (c) HMQC and (f) HMQC-SD-RFDR approaches, with small and large spheres representing the proximities of up to 3 Å and 4 Å, respectively.

HMQC-SD-RFDR experiment presented in this study requires shorter acquisition times than the 3D experiments to provide identical information, which is an added advantage.

The proposed HMQC-SD-RFDR approach has been applied to examine relayed $^{35}Cl\cdots^1H-^1H$ proximities in L-histidine.HCl.H$_2$O. A 1D ^{35}Cl NMR spectrum acquired with a QCPMG sequence is presented in Fig. S4 (Supporting Information) together with a lineshape fitting analysis to obtain the isotropic chemical shifts and quadrupolar coupling constants, as listed in Table S1. The narrow quadrupolar lineshape is due to the weak quadrupolar interaction associated with the chloride anions. Fig. 5 compares 2D $^1H-^{35}Cl$ D-HMQC spectra recorded without and with SD-RFDR pulses. In the conventional $^1H-^{35}Cl$ HMQC spectra of L-histidine.HCl.H$_2$O acquired with a short recoupling time of 265.6 µs (Fig. 5a), the 2D correlation peaks associated with closely proximate and dipolar coupled $^1H-^{35}Cl$ are observed for the Cl atoms and H1, H6 and H8, and Hw protons. The inter and intramolecular Cl$\cdots$H distances associated with Cl$\cdots$H1, Cl$\cdots$H6, Cl$\cdots$H7, Cl$\cdots$H8, and Cl $\cdots$ Hw are 2.20, 2.44, 2.94, 2.75 and 2.16 Å, respectively (Fig. 5c). Similar 2D peaks are observed for a 2D HMQC spectrum acquired with a recoupling time of 531.2 µs, shown in Fig. 5b; however, a weak intensity peak corresponding to Cl$\cdots$H5 (3.86 Å) appears. This indeed corroborates that the detection of the 2D $^{35}Cl-^1H$ peak for a Cl$\cdots$H distance closer to 4 Å is difficult to achieve in a conventional 2D HMQC experiment due to the weaker D_{Cl-H}. By combining heteronuclear $^{35}Cl\cdots^1H$ and homonuclear $^1H-^1H$ spin diffusion process, these weak intensity peaks are detected with much higher intensities, as shown in the HMQC-SD spectra presented in Fig. 5d and e. In addition, the enhanced uniformity of 2D peak intensities is apparent from these spectra, which indicates the addition of RFDR enables the detection of relayed $^{35}Cl-^1H-^1H$ peaks with an interatomic $^{35}Cl-^1H$ distance exceeding 3.8 Å (Fig. 5f).

Dopamine·HCl. Dopamine is a catecholamine derived from L-tyrosine, which has key biological significance as a neurotransmitter in the central nervous system and as a hormone in vesicles of the adrenal medulla that influences and controls the heartbeat rate, oxidative stress, and blood pressure [90,91]. The impaired dopamine metabolism and the absence of dopamine-containing neurons are associated with brain disorders such as Parkinson's disease [92]. In addition, dopamine is a food supplement (L-Dopa) that can be used as a direct precursor to increase the dopamine level in the body. In the presence of oxygen and alkaline/acidic environments, dopamine self-assembles into polydopamine (pDA) [93]. Care was taken to prevent the self-polymerization of dopamine by storing the powder form in a glass desiccator. To ensure that the dopamine characterized in this study is in monomeric form, liquid-state 1D ^1H and 2D $^1H-^1H$ and $^1H-^{13}C$ correlation NMR spectra were acquired and analyzed (Supporting Information, Figs. S5–S7): the narrow ^1H signals indicate the monomeric form of dopamine rather than the polymeric form. In the solid state, dopamine exists in different crystalline polymorphs such as neutral and zwitterionic forms, for which crystal structures have been previously solved [76,94]. Here, the solid-state form of dopamine·HCl is characterized by an NMR crystallography approach that combines solid-state NMR and periodic DFT calculations of previously published crystal structures. To further ensure that the dopamine preserved its molecular form, the GIPAW-DFT calculated chemical shifts for ^1H SQ, and DQ correlation peaks for all $^1H-^1H$ pairs (within 3 Å) in molecular and zwitterionic forms are overlaid on the experimental DQ-SQ peaks (Supporting Information, Fig. S8). A good agreement between the experimental ^1H SQ and DQ chemical shifts and the GIPAW-DFT calculated ^1H NMR chemical shifts is observed for the molecular form, but not for the zwitterionic form.

In Fig. 6 and 1D $^1H\{^{14}N\}$ and $^1H\{^{35}Cl\}$ HMQC spectra acquired with and without SD-RFDR blocks are compared with a single-pulse ^1H spectrum. The broad peak centered at ~7.6 ppm is due to an overlapped contribution from the NH$_2$ and aromatic protons. In the aliphatic region, the chemical shifts at 3.4 ppm and 5.9 ppm correspond to a CH$_2$ group next to the aromatic ring, and one of these protons is hydrogen-bonded to the oxygen atoms of the adjacent dopamine molecules. The peak at
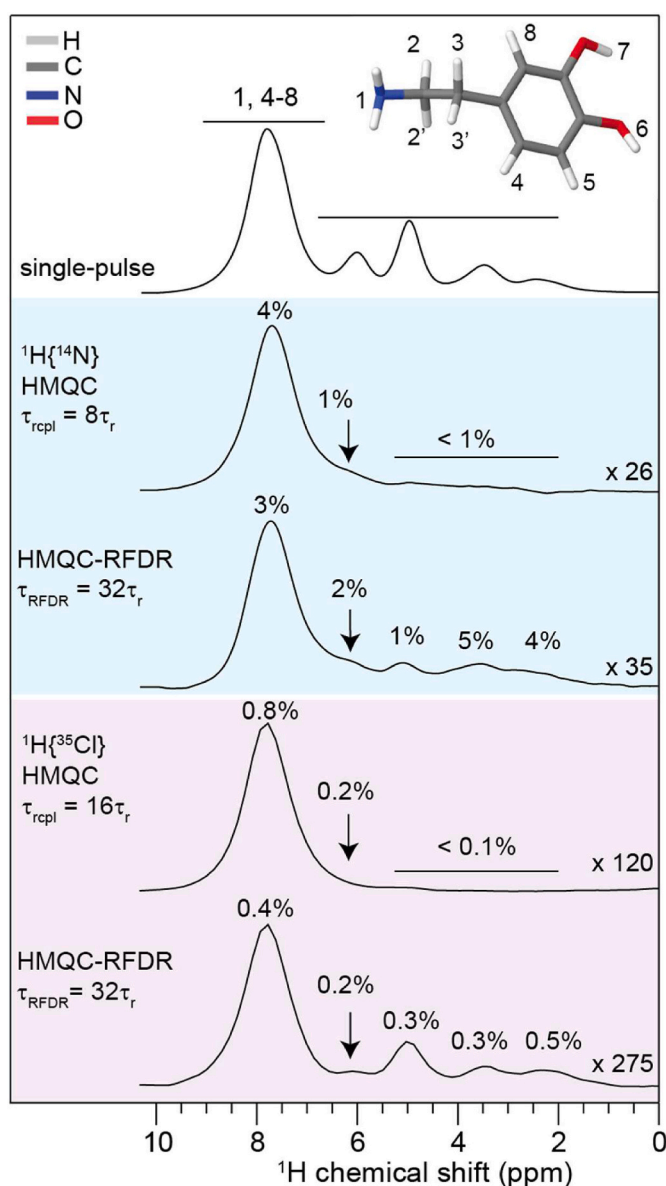

Fig. 6. Experimental ^1H NMR spectra are presented for dopamine·HCl: (top-to-bottom) single-pulse ^1H (900 MHz, 60.24 kHz MAS) spectrum, $^1H\{^{14}N\}$ HMQC-filtered ^1H spectrum acquired with τ_{RCPL} = 132.8 µs and with τ_{RFDR} = 531.2 µs (cyan shaded region), and $^1H\{^{35}Cl\}$ HMQC-filtered ^1H spectrum acquired with τ_{RCPL} = 265.6 µs and with τ_{RFDR} = 531.2 µs recoupling times (purple shaded region).

4.9 ppm corresponds to the CH$_2$ group next to the NH$_3$ group. The peak integral ratio of 7:4 associated with the signals at 6.5–9.5 ppm and 2.5–6.5 ppm further confirms the peak assignments. While all ^1H peaks are observed in the conventional ^1H spectrum, the $^1H\{^{14}N\}$-HMQC filtered 1D spectrum acquired with 132.8 µs of $^1H-^{14}N$ dipolar recoupling time using the SR4 sequence yields the ^1H signals of NH$_3$ peaks, and the ^1H signals of CH$_2$ protons are suppressed. For the same SR4 recoupling time, the addition of RFDR pulses (531.2 µs) leads to a ^1H NMR lineshape similar to that of the single-pulse experiment, i.e., the ^1H signal intensities in the 2.5–6.5 ppm range are enhanced. This trend is also evidenced in the $^1H\{^{35}Cl\}$ HMQC filtered experiments (τ_{rcpl} = 265.6 µs) with and without RFDR blocks, whereby the signals in the range of 2–7 ppm were only detected when an RDFR duration of 531.2 µs was added. Furthermore, 2D $^1H-^1H$ spin diffusion NMR spectra
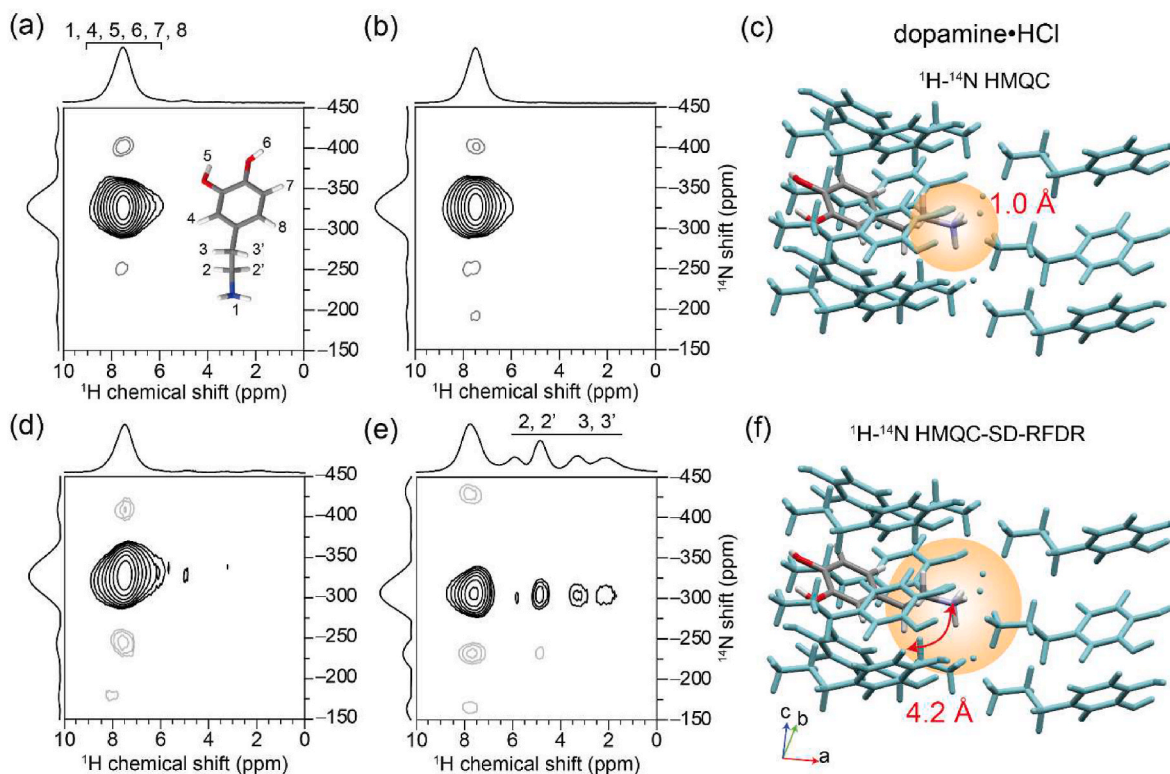
Fig. 7. Two-dimensional ^{1}H–^{14}N correlation spectra with skyline projections of dopamine·HCl acquired at 21.1 T and 60.24 kHz MAS with conventional HMQC (top) and HMQC-SD-RFDR pulse sequences (bottom), using SR4 recoupling for a τ_{RCPL} duration of (a, d, e) 132.8 μs and (b) 332 μs? RFDR durations were (d) 132.8 μs and (e) 1162 μs? The base contour levels are at 4% of the maximum peak height. Periodic DFT geometry optimized structures presented in (c) and (f) dopamine·HCl illustrate the short- and medium-range interactions probed by the HMQC and HMQC-SD-RFDR approaches. Spheres represent the long-range correlations of up to 4.2 Å between NH$_3$ groups and proton sites.

without and with RFDR pulses (Supporting Information, Fig. S9) are acquired and compared in order to highlight the role of RFDR pulses in enhancing the magnetization exchange between the neighboring ^{1}H sites in dopamine·HCl.

Conventional 2D ^{1}H–^{14}N HMQC spectra of dopamine·HCl acquired with different recoupling times of 132.8 μs and 332 μs are presented in Fig. 7a and b (top) together with the molecular packing interactions in the periodic DFT optimized crystal structure of dopamine·HCl. For both recoupling times, 2D peaks at ~7.6 ppm (^{1}H) and approximately −325 ppm (^{14}N) indicate that the short-range interactions between N1–H1 within the NH$_3^+$ groups are detected. However, 2D peaks corresponding to the long-range N–H correlations were not detected in the conventional HMQC experiment. In the HMQC-RFDR spectra shown in Fig. 7d and e (bottom), 2D peaks between ~ −325 ppm (^{14}N) and 2–6 ppm (^{1}H) indicate the relayed correlation signals enabled by the spin diffusion process.

We extend this analysis to probe the ^{1}H–^{35}Cl proximities in dopamine·HCl. A 1D ^{35}Cl NMR spectrum acquired with a QCPMG sequence is presented in Fig. S10 (Supporting Information) together with a lineshape fitting analysis. The isotropic chemical shift, quadrupolar coupling constant, and asymmetry parameter are listed in Table S2. In ^{1}H–^{35}Cl HMQC spectra of dopamine·HCl acquired with and without SD-RFDR blocks (Fig. 8), short and long-range correlations are observed. For a SR4 recoupling duration of 1024 μs (Fig. 8a), 2D peak at 7.6 ppm (^{1}H) and −150 to 10 ppm (^{35}Cl) is observed, which corresponds to the Cl–NH$_3^+$ and Cl–OHproximities with interatomic distances of ~2.2 Å. When RFDR pulses of duration 1024 μs are applied, 2D peaks between ^{35}Cl and CH$_2$ groups are also observed, as evident in Fig. 8b. The nearest internuclear ^{35}Cl–CH$_2$ (adjacent to NH$_2$) and ^{35}Cl–CH$_2$ (adjacent to the aromatic ring) distances are 3.5 and 3.7 Å, respectively. Although the 2D

HMQC-SD-RFDR approach enables the relayed correlation peaks to be detected, the measurement of interatomic distances from 2D volume integrals is less straightforward. In order to gain a quantitative insight into the distance constraints, a series of 2D experiments varying the heteronuclear recoupling time and spin diffusion mixing time would need to be acquired and the signal intensity buildup would need to be analyzed.

Further improvements to the proposed HMQC-SD-RFDR approach can be sought, for example, using the TRAPDOR-HMQC (TRAPDOR - transfer of population in double resonance) approach [42,95], by detecting the double-quantum (DQ) satellite transitions of quadrupolar nuclei. It has been shown that the DQ version is less sensitive to MAS instabilities and also benefits from a slightly higher resolution since the DQ chemical shift evolves at a frequency twice as large as the SQ chemical shifts. It has also been demonstrated that frequency-swept ^{14}N overtone CW-RESPDOR (continuous wave rotational-echo saturation-pulse double-resonance) experiments efficiently probe ^{1}H–^{14}N proximities with much longer internuclear distances than for the HMQC experiment [30]. The use of SD-RFDR block with CW-RESPDOR is expected to further extend the limit of detection of 2D peaks. Acceleration in the acquisition times can also be achieved at fast MAS by frequency selective (FS)-HMQC experiments, whereby selective excitation and detection of ^{1}H leads to a reduction in the inter-scan delays [41]. Notably, the proposed pulse sequence and its variants can be applied to detect ^{1}H–^{1}H and ^{1}H–^{14}N/^{35}Cl proximities in order to facilitate the structure elucidation of weak intermolecular interactions in organic molecules, reactive surfaces and interfaces of functional materials. It is to be noted that the SD transfer at fast spinning (>60 kHz MAS) may also be influenced by the chemical shift offset difference particularly when there is a small range of chemical-shift differences in the ^{1}H MAS spectra. It can be compensated by the addition of a spin lock,
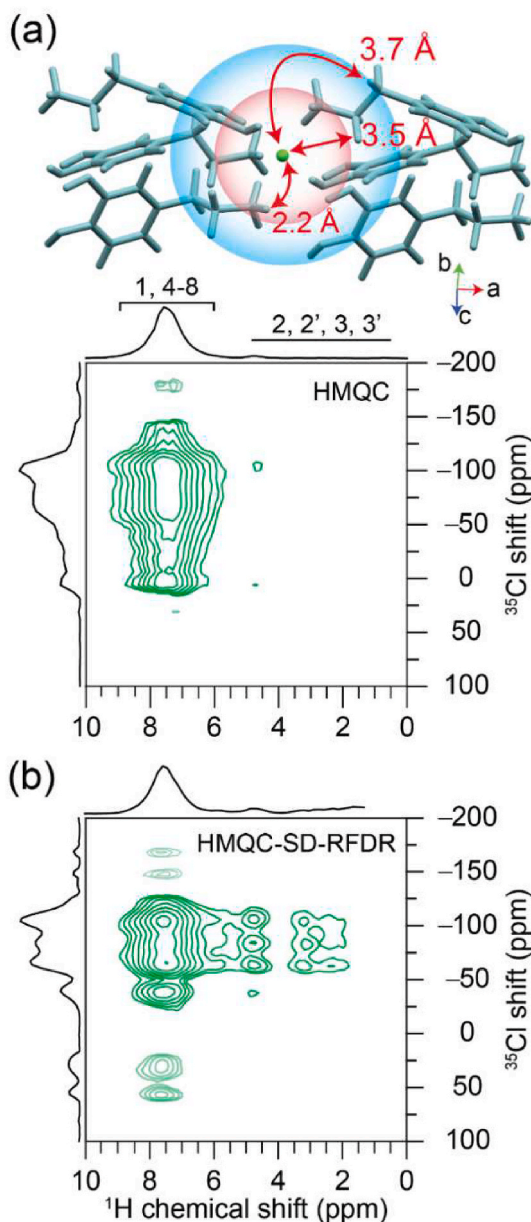
Fig. 8. Two-dimensional ^{1}H–^{35}Cl correlation spectra with skyline projection of dopamine·HCl acquired at 18.8 T and 62.5 kHz MAS with (a) conventional HMQC and (b) HMQC-SD-RFDR pulse sequences with SR4 recoupling of 1024 μs and τ_{RFDR} of 304 μs? In both cases, data were acquired with 128 coadded transients and 80 t_1 FIDs, corresponding to a total experimental time of 8.5 h each. The base contour levels are at 3% of the maximum peak height. A schematic representation of crystal packing in periodic DFT geometry optimized structures illustrating the short- and long-range interactions probed by the HMQC and HMQC-SD-RFDR approaches. Specifically, spheres represent the ^{1}H–^{35}Cl proximities within a distance of (a) 2.2 Å and (b) 3.7 Å.

although the short $T_{1\rho}$ of protons allows only short mixing times to be applied and long mixing times often reduce sensitivity. Reverse amplitude-modulated mixed rotational and rotary-resonance (AM-MIR-ROR) sequences can be tailored to compensate for offsets in the relevant range of chemical-shift differences, and these sequences also offer relatively high sensitivity compared to other sequences [84]. In addition, the reverse AM-MIRROR sequence requires lower rf fields than RFDR, and the optimum rf frequencies do not depend on the MAS frequency but only on the recoupled chemical-shift range.

4. Conclusions

This study presents a 2D HMQC-SD-RFDR experiment for probing the ^{1}H–^{1}H and ^{1}H-X (here, X = ^{14}N and ^{35}Cl) proximities in small organic molecules. A detailed analysis of 1D and 2D HMQC-SD-RFDR spectra is presented for L-histidine·HCl·H$_2$O and dopamine·HCl. The 1D version of the SD-HMQC sequence leads to spectral simplification by detecting ^{1}H {^{14}N} and ^{1}H{^{35}Cl} peaks for protons that are either *J*-coupled or dipolar coupled with ^{14}N or ^{35}Cl sites. By introducing an SD-RFDR block, ^{1}H peaks associated with ^{14}N–^{1}H–^{1}H and ^{35}Cl–^{1}H–^{1}H sites can be selectively excited and detected through relay transfer. Therefore, the spectral simplification in 1D spectra can be achieved by tuning the heteronuclear recoupling durations within the HMQC block as well as the spin diffusion time in the RFDR blocks. This can be simply achieved through the one-dimensional version of the proposed experiment. More elaborately, the proposed experiments can be used to acquire 2D ^{14}N-filtered ^{1}H–^{1}H spin-diffusion spectra and ^{1}H–^{14}N or ^{35}Cl–^{1}H correlation NMR spectra. Specifically, the 2D ^{1}H–^{14}N D-HMQC-SD-RFDR correlation experiment demonstrates a strong ability for observing remote ^{14}N–^{1}H correlations for which the N–H distances exceed 4 Å, which is difficult to achieve with the conventional ^{1}H–^{14}N HMQC experiment. The proposed approach particularly benefits from using higher magnetic field strengths under fast MAS conditions.

Declaration of competing interest

The authors declare that they have no known competing financial interests or personal relationships that could have appeared to influence the work reported in this paper.

Data availability

Data will be made available on request.

Appendix A. Supplementary data

Supplementary data to this article can be found online at https://doi.org/10.1016/j.ssnmr.2022.101808.

References

[1] M. Seifrid, G.N.M. Reddy, B.F. Chmelka, G.C. Bazan, Insight into the structures and dynamics of organic semiconductors through solid-state NMR spectroscopy, Nat. Rev. Mater. 5 (2020) 910–930, https://doi.org/10.1038/s41578-020-00232-5.

[2] D.J. Kubicki, S.D. Stranks, C.P. Grey, L. Emsley, NMR spectroscopy probes microstructure, dynamics and doping of metal halide perovskites, Nat. Rev. Chem 5 (2021) 624–645, https://doi.org/10.1038/s41570-021-00309-x.

[3] B. Reif, S.E. Ashbrook, L. Emsley, M. Hong, Solid-state NMR spectroscopy, Nat. Rev. Methods Prim. 1 (2021) 4, https://doi.org/10.1038/s43586-020-00004-z.

[4] A.B. Gunnarsdóttir, C.V. Amanchukwu, S. Menkin, C.P. Grey, Noninvasive in situ NMR study of "dead lithium" formation and lithium corrosion in full-cell lithium metal batteries, J. Am. Chem. Soc. 142 (2020) 20814–20827, https://doi.org/10.1021/jacs.0c10258.

[5] S.P. Brown, Advanced solid-state NMR methods for characterising structure and self-assembly in supramolecular chemistry, polymers and hydrogels, Curr. Opin. Colloid Interface Sci. 33 (2018) 86–98, https://doi.org/10.1016/j.cocis.2018.02.005.

[6] A. Marchetti, J. Chen, Z. Pang, S. Li, D. Ling, F. Deng, X. Kong, A. Marchetti, J. Chen, Z. Pang, X. Kong, S. Li, F. Deng, D. Ling, Understanding surface and interfacial chemistry in functional nanomaterials via solid-state NMR, Adv. Mater. 29 (2017), 1605895, https://doi.org/10.1002/adma.201605895.

[7] S. Ahlawat, K.R. Mote, N.A. Lakomek, V. Agarwal, Solid-state NMR: methods for biological solids, Chem. Rev. (2022), https://doi.org/10.1021/acs.chemrev.1c00852.

[8] P. Hodgkinson, NMR crystallography of molecular organics, Prog. Nucl. Magn. Reson. Spectrosc. 118–119 (2020) 10–53, https://doi.org/10.1016/j.pnmrs.2020.03.001.

[9] T. Charpentier, The PAW/GIPAW approach for computing NMR parameters: a new dimension added to NMR study of solids, Solid State Nucl. Magn. Reson. 40 (2011) 1–20, https://doi.org/10.1016/j.pnmrs.2020.03.001.

[10] N.T. Duong, Y. Aoyama, K. Kawamoto, T. Yamazaki, Y. Nishiyama, Structure solution of nano-crystalline small molecules using MicroED and solid-state NMR dipolar-based experiments, Molecules 26 (2021) 4652, https://doi.org/10.3390/molecules26154652.

[11] C. Guzmán-Afonso, Y.L. Hong, H. Colaux, H. Iijima, A. Saitow, T. Fukumura, Y. Aoyama, S. Motoki, T. Oikawa, T. Yamazaki, K. Yonekura, Y. Nishiyama, Understanding hydrogen-bonding structures of molecular crystals via electron and NMR nanocrystallography, Nat. Commun. 10 (2019) 3537, https://doi.org/10.1038/s41467-019-11469-2.

[12] D.H. Brouwer, S. Cadars, J. Eckert, Z. Liu, O. Terasaki, B.F. Chmelka, A general protocol for determining the structures of molecularly ordered but noncrystalline silicate frameworks, J. Am. Chem. Soc. 135 (2013) 5641–5655, https://doi.org/10.1021/ja311649m.

[13] A.L. Webber, L. Emsley, R.M. Claramunt, S.P. Brown, NMR crystallography of campho[2,3-c]pyrazole (Z' = 6): combining high-resolution ^{1}H-^{13}C solid-state MAS NMR spectroscopy and GIPAW chemical-shift calculations, J. Phys. Chem. 114 (2010) 10435–10442, https://doi.org/10.1021/jp104901j.

[14] C.J. Pickard, E. Salager, G. Pintacuda, B. Elena, L. Emsley, Resolving structures from powders by NMR crystallography using combined proton spin diffusion and plane wave DFT calculations, J. Am. Chem. Soc. 129 (2007) 8932–8933, https://doi.org/10.1021/ja071829h.

[15] B.R. Luginbuhl, P. Raval, T. Pawlak, Z. Du, T. Wang, N. Schopp, S. Chae, S. Yoon, A. Yi, H.J. Kim, V. Coropceanu, J.-L. Brédas, T.-Q. Nguyen, G.N.M. Reddy, Resolving atomic-scale interactions in nonfullerene acceptor organic solar cells with solid-state NMR spectroscopy, crystallographic modelling, and molecular dynamics simulations, Adv. Mater. 34 (2022), 2105943, https://doi.org/10.1002/adma.202105943.

[16] C.E. Hughes, G.N.M. Reddy, S. Masiero, S.P. Brown, P.A. Williams, K.D.M. Harris, Determination of a complex crystal structure in the absence of single crystals: analysis of powder X-ray diffraction data, guided by solid-state NMR and periodic DFT calculations, reveals a new 2'-deoxyguanosine structural motif, Chem. Sci. 8 (2017) 3971–3979, https://doi.org/10.1039/c7sc00587c.

[17] M. Cordova, M. Balodis, A. Hofstetter, F. Paruzzo, S.O. Nilsson Lill, E.S.E. Eriksson, P. Berruyer, B. Simões de Almeida, M.J. Quayle, S.T. Norberg, A. Svensk Ankarberg, S. Schantz, L. Emsley, Structure determination of an amorphous drug through large-scale NMR predictions, Nat. Commun. 12 (2021) 2964, https://doi.org/10.1038/s41467-021-23208-7.

[18] T. Pawlak, I. Sudgen, G. Bujacz, D. Iuga, S.P. Brown, M.J. Potrzebowski, Synergy of solid-state NMR, single-crystal X-ray diffraction, and crystal structure prediction methods: a case study of teriflunomide (TFM), cryst, Growth Des 21 (2021) 3328–3343, https://doi.org/10.1021/acs.cgd.1c00123.

[19] Z. Gan, J.P. Amoureux, J. Trébosc, Proton-detected ^{14}N MAS NMR using homonuclear decoupled rotary resonance, Chem. Phys. Lett. 435 (2007) 163–169, https://doi.org/10.1016/j.cplett.2006.12.066.

[20] R. Siegel, J. Trébosc, J.P. Amoureux, Z. Gan, 3D ^{1}H-^{13}C-^{14}N correlation solid-state NMR spectrum, J. Magn. Reson. 193 (2008) 321–325, https://doi.org/10.1016/j.jmr.2008.05.013.

[21] S. Cavadini, S. Antonijevic, A. Lupulescu, G. Bodenhausen, Indirect detection of nitrogen-14 in solids via protons by nuclear magnetic resonance spectroscopy, J. Magn. Reson. 182 (2006) 168–172, https://doi.org/10.1016/j.jmr.2006.06.003.

[22] Y. Nishiyama, Y. Endo, T. Nemoto, H. Utsumi, K. Yamauchi, K. Hioka, T. Asakura, Very fast magic angle spinning ^{1}H-^{14}N 2D solid-state NMR: sub-micro-liter sample data collection in a few minutes, J. Magn. Reson. 208 (2011) 44–48, https://doi.org/10.1016/j.jmr.2010.10.001.

[23] S. Cavadini, Indirect detection of nitrogen-14 in solid-state NMR spectroscopy, Prog. Nucl. Magn. Reson. Spectrosc. 56 (2010) 46–77, https://doi.org/10.1016/j.pnmrs.2009.08.001.

[24] H. Nagashima, J. Trébosc, J. Trébosc, Y. Kon, K. Sato, O. Lafon, O. Lafon, J. P. Amoureux, J.P. Amoureux, J.P. Amoureux, Observation of low-γ quadrupolar nuclei by surface-enhanced NMR spectroscopy, J. Am. Chem. Soc. 142 (2020) 10659–10672, https://doi.org/10.1021/jacs.9b13838.

[25] O. Lafon, Q. Wang, B. Hu, F. Vasconcelos, J. Trébosc, S. Cristol, F. Deng, J. P. Amoureux, Indirect detection via spin-1/2 nuclei in solid state NMR spectroscopy: application to the observation of proximities between protons and quadrupolar nuclei, J. Phys. Chem. 113 (2009) 12864–12878, https://doi.org/10.1021/jp906099k.

[26] M. Concistré, I. Kuprov, I.M. Haies, P.T. Williamson, M. Carravetta, ^{14}N overtone NMR under MAS: signal enhancement using cross-polarization methods, J. Magn. Reson. 298 (2019) 1–5, https://doi.org/10.1016/j.jmr.2018.10.017.

[27] Y. Nishiyama, M. Malon, Z. Gan, Y. Endo, T. Nemoto, Proton-nitrogen-14 overtone two-dimensional correlation NMR spectroscopy of solid-sample at very fast magic angle sample spinning, J. Magn. Reson. 230 (2013) 160–164, https://doi.org/10.1016/j.jmr.2013.02.015.

[28] D. Carnevale, M. Hollenstein, G. Bodenhausen, Self-Assembly of DNA and RNA building blocks explored by nitrogen-14 NMR crystallography: structure and dynamics, ChemPhysChem 21 (2020) 1044–1051, https://doi.org/10.1002/cphc.201901214.

[29] J.A. Jarvis, M. Concistre, I.M. Haies, R.W. Bounds, I. Kuprov, M. Carravetta, P.T. F. Williamson, Quantitative analysis of ^{14}N quadrupolar coupling using ^{1}H detected ^{14}N solid-state NMR, Phys. Chem. Chem. Phys. 21 (2019) 5941–5949, https://doi.org/10.1039/c8cp06276e.

[30] N.T. Duong, Y. Nishiyama, Detection of remote proton–nitrogen correlations by ^{1}H-detected ^{14}N overtone solid-state NMR at fast MAS, Phys. Chem. Chem. Phys. (2022), https://doi.org/10.1039/d2cp00155a.

[31] I.M. Haies, J.A. Jarvis, H. Bentley, I. Heinmaa, I. Kuprov, P.T.F. Williamson, M. Carravetta, ^{14}N overtone NMR under MAS: signal enhancement using symmetry-based sequences and novel simulation strategies, Phys. Chem. Chem. Phys. 17 (2015) 6577–6587, https://doi.org/10.1039/c4cp03994g.

[32] M.K. Pandey, Y. Nishiyama, A one-dimensional solid-state NMR approach for ^{14}NH/^{14}NH overtone correlation through ^{1}H/^{1}H mixing under fast MAS, Phys. Chem. Chem. Phys. 20 (2018) 25849–25853, https://doi.org/10.1039/c8cp05000g.

[33] X. Lu, O. Lafon, J. Trébosc, G. Tricot, L. Delevoye, F. Méar, L. Montagne, J. P. Amoureux, Observation of proximities between spin-1/2 and quadrupolar nuclei: which heteronuclear dipolar recoupling method is preferable? J. Chem. Phys. 137 (2012), 144201 https://doi.org/10.1063/1.4753987.

[34] G.N.M. Reddy, A. Marsh, J.T. Davis, S. Masiero, S.P. Brown, Interplay of noncovalent interactions in ribbon-like Guanosine self-assembly: an NMR crystallography study, Cryst. Growth Des. 15 (2015) 5945–5954, https://doi.org/10.1021/acs.cgd.5b01440.

[35] G.N.M. Reddy, D.S. Cook, D. Iuga, R.I. Walton, A. Marsh, S.P. Brown, An NMR crystallography study of the hemihydrate of 2', 3'-O-isopropylideneguanosine, Solid State Nucl. Magn. Reson. 65 (2015) 41–48, https://doi.org/10.1016/j.ssnmr.2015.01.001.

[36] G.N.M. Reddy, M. Malon, A. Marsh, Y. Nishiyama, S.P. Brown, Fast magic-angle spinning three-dimensional NMR experiment for simultaneously probing H-H and N-H proximities in solids, Anal. Chem. 88 (2016) 11412–11419, https://doi.org/10.1021/acs.analchem.6b01869.

[37] M. Grüne, R. Luxenhofer, D. Iuga, S.P. Brown, A.C. Pöppler, ^{14}N–^{1}H HMQC solid-state NMR as a powerful tool to study amorphous formulations – an exemplary study of paclitaxel loaded polymer micelles, J. Mater. Chem. B. 8 (2020) 6827–6836, https://doi.org/10.1039/d0tb00614a.

[38] Y.L. Hong, G.N.M. Reddy, Y. Nishiyama, Selective detection of active pharmaceutical ingredients in tablet formulations using solid-state NMR spectroscopy, Solid State Nucl. Magn. Reson. 106 (2020), 101651, https://doi.org/10.1016/j.ssnmr.2020.101651.

[39] D. Iuga, E.K. Corlett, S.P. Brown, ^{35}Cl–^{1}H Heteronuclear correlation magic-angle spinning nuclear magnetic resonance experiments for probing pharmaceutical salts, Magn. Reson. Chem. 59 (2021) 1089–1100, https://doi.org/10.1002/mrc.5188.

[40] M.K. Pandey, H. Kato, Y. Ishii, Y. Nishiyama, Two-dimensional proton-detected ^{35}Cl/^{1}H correlation solid-state NMR experiment under fast magic angle sample spinning: application to pharmaceutical compounds, Phys. Chem. Chem. Phys. 18 (2016) 6209–6216, https://doi.org/10.1039/c5cp06042g.

[41] A.V. Wijesekara, A. Venkatesh, B.J. Lampkin, B. VanVeller, J.W. Lubach, K. Nagapudi, I. Hung, P.L. Gor'kov, Z. Gan, A.J. Rossini, Fast acquisition of proton-detected HETCOR solid-state NMR spectra of quadrupolar nuclei and rapid measurement of NH bond lengths by frequency selective HMQC and RESPDOR pulse sequences, Chem. Eur. J. 26 (2020) 7881–7888, https://doi.org/10.1002/chem.202000390.

[42] I. Hung, Z. Gan, High-resolution NMR of S = 3/2 quadrupole nuclei by detection of double-quantum satellite transitions via protons, J. Phys. Chem. Lett. 11 (2020) 4734–4740, https://doi.org/10.1021/acs.jpclett.0c01236.

[43] M.J. Bayro, R. Ramachandran, M.A. Caporini, M.T. Eddy, R.G. Griffin, Radio frequency-driven recoupling at high magic-angle spinning frequencies: homonuclear recoupling sans heteronuclear decoupling, J. Chem. Phys. 128 (2008), 052321, https://doi.org/10.1063/1.2834732.

[44] M. Roos, V.S. Mandala, M. Hong, Determination of long-range distances by fast magic-angle-spinning radiofrequency-driven ^{19}F-^{19}F dipolar recoupling NMR, J. Phys. Chem. B 122 (2018) 9302–9313, https://doi.org/10.1021/acs.jpcb.8b06878.

[45] A. Ramamoorthy, J. Xu, 2D ^{1}H/^{1}H RFDR and NOESY NMR experiments on a membrane-bound antimicrobial peptide under magic angle spinning, J. Phys. Chem. B 117 (2013) 6693–6700, https://doi.org/10.1021/jp4034003.

[46] L.A. Straasø, R. Shankar, K.O. Tan, J. Hellwagner, B.H. Meier, M.R. Hansen, N. C. Nielsen, T. Vosegaard, M. Ernst, A.B. Nielsen, Improved transfer efficiencies in radio-frequency-driven recoupling solid-state NMR by adiabatic sweep through the dipolar recoupling condition, J. Chem. Phys. 145 (2016), 034201, https://doi.org/10.1063/1.4958318.

[47] B. Elena, L. Emsley, Powder crystallography by proton solid-state NMR spectroscopy, J. Am. Chem. Soc. 127 (2005) 9140–9146, https://doi.org/10.1021/ja051208t.

[48] B. Elena, G. Pintacuda, N. Mifsud, L. Emsley, Molecular structure determination in powders by NMR crystallography from proton spin diffusion, J. Am. Chem. Soc. 128 (2006) 9555–9560, https://doi.org/10.1021/ja062353p.

[49] M.G. Jain, D. Lalli, J. Stanek, C. Gowda, S. Prakash, T.S. Schwarzer, T. Schubeis, K. Castiglione, L.B. Andreas, P.K. Madhu, G. Pintacuda, V. Agarwal, Selective ^{1}H-^{1}H distance restraints in fully protonated proteins by very fast magic-angle spinning solid-state NMR, J. Phys. Chem. Lett. 8 (2017) 2399–2405, https://doi.org/10.1021/acs.jpclett.7b00983.

[50] A. Karki, J. Vollbrecht, A.J. Gillett, S.S. Xiao, Y. Yang, Z. Peng, N. Schopp, A. L. Dixon, S. Yoon, M. Schrock, H. Ade, G.N.M. Reddy, R.H. Friend, T.Q. Nguyen, The role of bulk and interfacial morphology in charge generation, recombination, and extraction in non-fullerene acceptor organic solar cells, Energy Environ. Sci. 13 (2020) 3679–3692, https://doi.org/10.1039/d0ee01896a.

[51] A. Karki, J. Vollbrecht, A.L. Dixon, N. Schopp, M. Schrock, G.N.M. Reddy, T.-Q. Nguyen, Understanding the high performance of over 15% efficiency in single-junction bulk heterojunction organic solar cells, Adv. Mater. 31 (2019), 1903868, https://doi.org/10.1002/adma.201903868.

[52] S. Samanta, P. Raval, G.N.M. Reddy, D. Chaudhuri, Cooperative self-assembly driven by multiple noncovalent interactions: investigating molecular origin and reassessing characterization, ACS Cent. Sci. 7 (2021) 1391–1399, https://doi.org/10.1021/acscentsci.1c00604.

[53] G.N.M. Reddy, P. Selter, Y. Makita, S. Arai, M. Miyagawa, H. Nakano, H. Wang, J. A. Gerbec, F. Shimizu, B.F. Chmelka, Nanoscale surface compositions and structures of plasma-modified poly(ethylene terephthalate) thin films, J. Phys. Chem. C 125 (2021) 20658–20669, https://doi.org/10.1021/acs.jpcc.1c06658.

[54] Z. Du, M. Mainville, J. Vollbrecht, A.L. Dixon, N. Schopp, M. Schrock, Z. Peng, J. Huang, S. Chae, H. Ade, M. Leclerc, G.N.M. Reddy, T.Q. Nguyen, Insights into bulk-heterojunction organic solar cells processed from green solvent, Sol. RRL. 5 (2021), 2100213, https://doi.org/10.1002/solr.202100213.

[55] P. Raval, R.M. Kennard, E.S. Vasileiadou, C.J. Dahlman, I. Spanopoulos, M. L. Chabinyc, M. Kanatzidis, G.N.M. Reddy, Understanding instability in formamidinium lead halide perovskites: kinetics of transformative reactions at Grain and subgrain boundaries, ACS Energy Lett. 7 (2022) 1534–1543, https://doi.org/10.1021/acsenergylett.2c00140.

[56] C.J. Dahlman, R.M. Kennard, P. Paluch, N.R. Venkatesan, M.L. Chabinyc, G.N. M. Reddy, Dynamic motion of organic spacer cations in ruddlesden–popper lead iodide perovskites probed by solid-state NMR spectroscopy, Chem. Mater. 33 (2021) 642–656, https://doi.org/10.1021/acs.chemmater.0c03958.

[57] M. Li, W. Xu, Y. Su, Solid-state NMR spectroscopy in pharmaceutical sciences, TrAC - Trends Anal. Chem. 135 (2021), 116152, https://doi.org/10.1016/j.trac.2020.116152.

[58] R. Linser, B. Bardiaux, V. Higman, U. Fink, B. Reif, Structure calculation from unambiguous long-range amide and methyl ^{1}H-^{1}H distance restraints for a microcrystalline protein with MAS solid-state NMR spectroscopy, J. Am. Chem. Soc. 133 (2011) 5905–5912, https://doi.org/10.1021/ja110222h.

[59] C.J. Dahlman, D.J. Kubicki, G.N.M. Reddy, Interfaces in metal halide perovskites probed by solid-state NMR spectroscopy, J. Mater. Chem. A. 9 (2021) 19206–19244, https://doi.org/10.1039/d1ta03572j.

[60] M.J. Bayro, T. Maly, N.R. Birkett, C.M. Dobson, R.G. Griffin, M.J. Bayro, T. Maly, R. G. Griffin, N.R. Birkett, C.M. Dobson, Long-range correlations between aliphatic ^{13}C nuclei in protein MAS NMR spectroscopy, Angew. Chem. Int. Ed. 48 (2009) 5708–5710, https://doi.org/10.1002/anie.200901520.

[61] S.P. Brown, Applications of high-resolution ^{1}H solid-state NMR, Solid State Nucl. Magn. Reson. 41 (2012) 1–27, https://doi.org/10.1016/j.ssnmr.2011.11.006.

[62] A.L. Dixon, H. Vezin, T.-Q. Nguyen, G.N.M. Reddy, Structural insights into Lewis acid- and F4TCNQ-doped conjugated polymers by solid-state magnetic resonance spectroscopy, Mater. Horiz. 9 (2022) 981–990, https://doi.org/10.1039/d1mh01574e.

[63] A. Krishna, H. Zhang, Z. Zhou, T. Gallet, M. Dankl, O. Ouellette, F.T. Eickemeyer, F. Fu, S. Sanchez, M. Mensi, S.M. Zakeeruddin, U. Rothlisberger, G.N. Manjunatha Reddy, A. Redinger, M. Grätzel, A. Hagfeldt, Nanoscale interfacial engineering enables highly stable and efficient perovskite photovoltaics, Energy Environ. Sci. 14 (2021) 5552–5562, https://doi.org/10.1039/D1EE02454J.

[64] M.A.A. Kazemi, P. Raval, K. Cherednichenko, J.-N. Chotard, A. Krishna, A. Demortiere, G.N.M. Reddy, F. Sauvage, Molecular-level insight into correlation between surface defects and stability of methylammonium lead halide perovskite under controlled humidity, Small Methods 5 (2021), 2000834, https://doi.org/10.1002/smtd.202000834.

[65] E. Salager, R.S. Stein, C.J. Pickard, B. Elena, L. Emsley, Powder NMR crystallography of thymol, Phys. Chem. Chem. Phys. 11 (2009) 2610–2621, https://doi.org/10.1039/b821018g.

[66] E. Salager, G.M. Day, R.S. Stein, C.J. Pickard, B. Elena, L. Emsley, Powder crystallography by combined crystal structure prediction and high-resolution ^{1}H solid-state NMR spectroscopy, J. Am. Chem. Soc. 132 (2010) 2564–2566, https://doi.org/10.1021/ja909449h.

[67] M. Roos, T. Wang, A.A. Shcherbakov, M. Hong, Fast magic-angle-spinning ^{19}F spin exchange NMR for determining nanometer ^{19}F-^{19}F distances in proteins and pharmaceutical compounds, J. Phys. Chem. B 122 (2018) 2900–2911, https://doi.org/10.1021/acs.jpcb.8b00310.

[68] M. Hong, K. Schmidt-Rohr, Magic-angle-spinning NMR techniques for measuring long-range distances in biological macromolecules, Acc. Chem. Res. 46 (2013) 2154–2163, https://doi.org/10.1021/ar300294x.

[69] I. Hung, Z. Gan, On the practical aspects of recording wideline QCPMG NMR spectra, J. Magn. Reson. 204 (2010) 256–265, https://doi.org/10.1016/j.jmr.2010.03.001.

[70] S. Hayashi, K. Hayamizu, Chemical shift standards in high-resolution solid-state NMR (1) ^{13}C, ^{29}Si, and ^{1}H nuclei, Bull. Chem. Soc. Jpn. 64 (1991) 685–687, https://doi.org/10.1246/bcsj.64.685.

[71] G.E. Martin, C.E. Hadden, Long-range ^{1}H-^{15}N heteronuclear shift correlation at natural abundance, J. Nat. Prod. 63 (2000) 543–585, https://doi.org/10.1021/np9903191.

[72] R.K. Harris, E.D. Becker, S.M. Cabral De Menezes, P. Granger, R.E. Hoffman, K. W. Zilm, Further conventions for NMR shielding and chemical shifts IUPAC recommendations 2008, Solid State Nucl. Magn. Reson. 33 (2008) 41–56, https://doi.org/10.1016/j.ssnmr.2008.02.004.

[73] A. Brinkmann, A.P.M. Kentgens, Proton-selective ^{17}O-^{1}H distance measurements in fast magic-angle-spinning solid-state NMR spectroscopy for the determination of hydrogen bond lengths, J. Am. Chem. Soc. 128 (2006) 14758–14759, https://doi.org/10.1021/ja065415k.

[74] A.E. Bennett, J.H. Ok, R.G. Griffin, S. Vega, Chemical shift correlation spectroscopy in rotating solids: radio frequency-driven dipolar recoupling and longitudinal exchange, J. Chem. Phys. 96 (1992) 8624–8627, https://doi.org/10.1063/1.462267.

[75] K. Oda, H. Koyama, A refinement of the crystal structure of histidine hydrochloride monohydrate, Acta Crystallogr. B28 (1972) 639–642, https://doi.org/10.1107/s0567740872002894.

[76] R. Bergin, D. Carlström, The structure of the catecholamines. II. The crystal structure of dopamine hydrochloride, Acta Crystallogr. B24 (1968) 1506–1510, https://doi.org/10.1107/s0567740868004553.

[77] C.J. Pickard, F. Mauri, All-electron magnetic response with pseudopotentials: NMR chemical shifts, Phys. Rev. B 63 (2001), 245101, https://doi.org/10.1103/PhysRevB.63.245101.

[78] J.R. Yates, C.J. Pickard, F. Mauri, Calculation of NMR chemical shifts for extended systems using ultrasoft pseudopotentials, Phys. Rev. B Condens. Matter 76 (2007), 024401, https://doi.org/10.1103/PhysRevB.76.024401.

[79] S.J. Clark, M.D. Segall, C.J. Pickard, P.J. Hasnip, M.I.J. Probert, K. Refson, M. C. Payne, First principles methods using CASTEP, Zeitschrift Fur Krist 220 (2005) 567–570, https://doi.org/10.1524/zkri.220.5.567.65075.

[80] A. Tkatchenko, M. Scheffler, Accurate molecular van der Waals interactions from ground-state electron density and free-atom reference data, Phys. Rev. Lett. 102 (2009), 073005, https://doi.org/10.1103/PhysRevLett.102.073005.

[81] D. Vanderbilt, Soft self-consistent pseudopotentials in a generalized eigenvalue formalism, Phys. Rev. B 41 (1990) 7892, https://doi.org/10.1103/PhysRevB.41.7892.

[82] E. Nehra, N. Sehrawat, T. Kobayashi, Y. Nishiyama, M.K. Pandey, Proton-detected ^{15}N-^{1}H dipolar coupling/^{1}H chemical shift correlation experiment for the measurement of NH distances in biological solids under fast MAS solid-state NMR, J. Magn. Reson. Open. 10– 11 (2022), 100028, https://doi.org/10.1016/j.jmro.2021.100028.

[83] S. Li, M. Hong, Protonation, tautomerization, and rotameric structure of histidine: a comprehensive study by magic-angle-spinning solid-state NMR, J. Am. Chem. Soc. 133 (2011) 1534–1544, https://doi.org/10.1021/ja108943n.

[84] J.J. Wittmann, V. Agarwal, J. Hellwagner, A. Lends, R. Cadalbert, B.H. Meier, M. Ernst, Accelerating proton spin diffusion in perdeuterated proteins at 100 kHz MAS, J. Biomol. NMR 66 (2016) 233–242, https://doi.org/10.1007/s10858-016-0071-8.

[85] O. Lafon, A.S.L. Thankamony, T. Kobayashi, D. Carnevale, V. Vitzthum, I. I. Slowing, K. Kandel, H. Vezin, J.P. Amoureux, G. Bodenhausen, M. Pruski, Mesoporous silica nanoparticles loaded with surfactant: low temperature magic angle spinning ^{13}C and ^{29}Si NMR enhanced by dynamic nuclear polarization, J. Phys. Chem. C 117 (2013) 1375–1382, https://doi.org/10.1021/jp310109s.

[86] A. Venkatesh, I. Hung, K.C. Boteju, A.D. Sadow, P.L. Gor'kov C, Z. Gan, A. J. Rossini, Suppressing ^{1}H spin diffusion in fast MAS proton detected heteronuclear correlation solid-state NMR experiments, Solid State Nucl. Magn. Reson. 105 (2020), 101636, https://doi.org/10.1016/j.ssnmr.2019.101636.

[87] A.S. Tatton, T.N. Pham, F.G. Vogt, D. Iuga, A.J. Edwards, S.P. Brown, Probing intermolecular interactions and nitrogen protonation in pharmaceuticals by novel ^{15}N-edited and 2D ^{14}N-^{1}H solid-state NMR, CrystEngComm 14 (2012) 2654–2659, https://doi.org/10.1039/c2ce06547a.

[88] R. Zhang, M.K. Pandey, Y. Nishiyama, A. Ramamoorthy, A novel high-resolution and sensitivity-enhanced three-dimensional solid-state NMR experiment under ultrafast magic angle spinning conditions, Sci. Rep. 5 (2015), 11810, https://doi.org/10.1038/srep11810.

[89] X. Lu, D. Skomski, K.C. Thompson, M.J. McNevin, W. Xu, Y. Su, Three-dimensional NMR spectroscopy of fluorinated pharmaceutical solids under ultrafast magic angle spinning, Anal. Chem. 91 (2019) 6217–6224, https://doi.org/10.1021/acs.analchem.9b00884.

[90] H.J. Olguín, D.C. Guzmán, E.H. García, G.B. Mejía, The role of dopamine and its dysfunction as a consequence of oxidative stress, Oxid. Med. Cell. Longev. (2016), 9730467, https://doi.org/10.1155/2016/9730467, 2016.

[91] R. Brisch, A. Saniotis, R. Wolf, H. Bielau, H.G. Bernstein, J. Steiner, B. Bogerts, K. Braun, J. Kumaratilake, M. Henneberg, T. Gos, The role of dopamine in schizophrenia from a neurobiological and evolutionary perspective: old fashioned, but still in vogue, Front. Psychiatr. 5 (2014) 47, https://doi.org/10.3389/fpsyt.2014.00047.

[92] D. Bora Da, L. Scheffer, F.C. Freitas, A.S. Aguiar, C. Ward, L. Guilherme, A. Guglielmo, R.D. Prediger, S.J.F. Cronin, R. Walz, N.A. Andrews, A. Latini, Impaired dopamine metabolism is linked to fatigability in mice and fatigue in

Parkinson's disease patients, Brain Commun 3 (2021), https://doi.org/10.1093/braincomms/fcab116 fcab116.

[93] T.P. Chen, T. Liu, T.L. Su, J. Liang, Self-polymerization of dopamine in acidic environments without oxygen, Langmuir 33 (2017) 5863–5871, https://doi.org/10.1021/acs.langmuir.7b01127.

[94] L. Cruickshank, A.R. Kennedy, N. Shankland, Tautomeric and ionisation forms of dopamine and tyramine in the solid state, J. Mol. Struct. 1051 (2013) 132–136, https://doi.org/10.1016/j.molstruc.2013.08.002.

[95] R. Bayzou, J. Trébosc, I. Hung, Z. Gan, O. Lafon, J.P. Amoureux, Indirect NMR detection via proton of nuclei subject to large anisotropic interactions, such as ^{14}N, ^{195}Pt, and ^{35}Cl, using the T-HMQC sequence, J. Chem. Phys. 156 (2022), 064202, https://doi.org/10.1063/5.0082700.